BENEFIT STUDIES FOR ROTOR WITH ACTIVE TWIST CONTROL USING WEAK FLUID-STRUCTURE COUPLING

Q. Zhang[1], F. Hoffmann[2] and B. G. van der Wall[2]
[1] DLR, Institute of Aerodynamics and Flow Technology
[2] DLR, Institute of Flight Systems
Braunschweig, Germany

Abstract

This paper presents the results of the numerical benefit studies concerning a rotor with implemented active twist control technology which was defined in the framework of the European FRIENDCOPTER project. The objective is to demonstrate the potential improvement of the active twist rotor with respect to rotor aerodynamic performance, noise and vibration reduction. The numerical method applied for the benefit studies is based on a weak coupling procedure between the DLR rotor simulation code S4 and the DLR Navier-Stokes flow solver FLOWer. In this study, the weak coupling approach was applied to two steady forward flight cases at advance ratios of 0.318 and 0.378. The numerical results showed that applying optimized active twist control laws, the vibration and power consumption level of the active twist rotor can be reduced substantially in both cases.

NOMENCLATURE

C_nM^2	sectional normal force coefficient
C_tM^2	sectional tangential force coefficient
C_mM^2	sectional pitch moment coefficient
M	Mach number
α_{sh}	rotor shaft angle [°]
μ	advance ratio
θ_0	collective pitch angle [°]
θ_{1C}	longitudinal cyclic pitch [°]
θ_{1S}	lateral cyclic pitch [°]
ψ	azimuth angle [°]
Ω	rotor rotational frequency [rad/s]

ACRONYMS

BVI	Blade Vortex Interaction
CFD	Computational Fluid Dynamics
CSM	Computational Structure Mechanics
DLR	Deutsches Zentrum für Luft- und Raumfahrt e.V.
HHC	Higher Harmonic Control
HOST	Helicopter Overall Simulation Tool
IAG	Institut für Aerodynamik und Gasdynamik, University of Stuttgart
IBC	Individual Blade Control
MFC	Macro Fiber Composite

1. INTRODUCTION

In recent years, active material technology has been applied for helicopter main rotors to counteract adverse aeroelastic and acoustic effects [1][2][3][4][5]. In the active control concepts, the rotor control is integrated into the blade structure, such that a local influence of the blade aerodynamics can be achieved. In case of a conventional rotor, a certain trim state is achieved by the collective and cyclic pitch input via the swash plate, where the swash plate only allows for static (collective) and 1/rev cyclic control inputs. The advantage of active rotor control is that Higher Harmonic Controls (HHC) at n/rev, n=2,3,4,…, can be introduced into the rotor blade individually, such that the trim state is not uniquely correlated to a certain control input at the swash plate. This feature of the active rotor control can be used for performance increase, noise and vibration reduction.

For helicopter main rotors, active control methods like the active twist [1][2] or the active trailing edge flap [3][4][5] are the two most popular smart blade concepts. Active twist control concepts are based on the actively twisting of a part of the rotor blade. In the framework of the European project FRIENDCOPTER, DLR has developed an active twist model rotor [6] which has been successfully tested on a whirl tower [7]. As a part of the work package within the FRIENDCOPTER project, the potentials of the active twist rotor with respect to vibration reduction and performance increase should be assessed using computational simulations. Applying a weak-coupled CFD/CSM method, a trimmed steady-state flight condition of the isolated rotor can be obtained. The rotors with and without active twist control (denoted as the active and the passive rotors, respectively) can be trimmed to an identical flight condition, such that it allows for a meaningful comparison between the active and passive rotors.

The objective of the present paper is to investigate the potentials of the active twist model rotor regarding the reduction of vibration (test case 1) and power consumption (test case 2) under steady forward flight conditions.

2. NUMERICAL METHODS

2.1. Rotor Simulation Code S4

S4 is a rotor simulation code developed at the Institute of Flight Systems of DLR, with a first description and application to the work concerning the Higher Harmonic Control of a hingeless rotor [8]. As a flight mechanics tool, it is capable of trimming isolated rotors to prescribed non-rotating hub forces and moments. The S4 code mainly consists of three modules: the aerodynamics, the structural dynamics and induced velocity module, the latter with different levels of sophistication.

In this application the blade is discretized radially into 20 elements of decreasing size towards the tip. For each of these elements, local aerodynamic forces and moments are calculated based on a lifting-line method. Local forces and moments are then summed up into the generalized forces of the respective blade modes. In the structural dynamics module, the blade is described by its flap, lead-lag and torsion modes in terms fo their shape and associated natural frequencies. The generalized coordinates of each mode are computed according to the generalized aerodynamic forces by means of a Runge-Kutta time-marching integration scheme of 4^{th} order with an azimuthal resolution of 2deg.

The induced velocities are computed using a modified version of Beddoes prescribed wake geometry [9], taking account of the effect of harmonic air loads on the wake convection normal to the rotor disk [10]. This allows to compute the BVI location and associated high-frequency air loads, which are responsible for BVI noise radiation.

2.2. CFD Solver FLOWer

The CFD code FLOWer [11] is a block structured flow solver based on a cell-centred finite volume discretization. FLOWer solves the 3D unsteady Reynolds-averaged Navier-Stokes (RANS) equations which are formulated in the hub attached rotating frame of reference. In the current study, central schemes are applied for the spatial discretization, where the spurious oscillations are suppressed by first and second order artificial dissipation. Time accurate computations are performed via dual time stepping with a second order implicit time integration operator [12]. A speed-up of the computations is achieved by the multi-grid technique. Turbulence effects are taken into account by a slightly modified Wilcox two-equation k-ω model. The blade motion is realized using the Chimera-technique [13] implemented in FLOWer. All CFD simulations in this report were performed with the FLOWer release version 2008.1.

2.3. Weak Coupling

The motivation for applying the weak coupling procedure is to replace the aerodynamic forces and moments which were calculated in the S4 code (based on 2D lifting line theory) by 3D CFD aerodynamics.

The iterative weak coupling approach starts from an initial trimmed solution of S4, which is denoted as the 0^{th} iteration. The blade deformation is described by a limited set of mode shapes together with their deflections:

$$h(r,\psi)=\sum_{i=1}^{n} q_i(\psi)\cdot \hat{h}_i(r) \tag{1}$$

where n is the number of modes, $q_i(\psi)$ the generalized coordinate of the i^{th} mode (represented by a Fourier series up to the 9^{th} harmonic) and $h_i(r)$ is the associated mode shape (represented by a polynomial of 6^{th} order in the radial coordinate).

The collective control angle θ_0, the cyclic control angles θ_{1c} and θ_{1s}, as well as the blade dynamic response in flap, lead-lag and torsion given by Eq. (1) are passed over to FLOWer. In the FLOWer code, the given elastic deflections and the control angles of the 0^{th} iteration are used to reconstruct the 3D elastic deformed rotor blades in the CFD mesh. Based on the prescribed blade geometry and the given operational conditions, an unsteady RANS calculation is performed with FLOWer, until a periodic flow state is obtained and all transients have died out. Subsequently, the distributions of aerodynamic loads from the FLOWer calculation, i.e., the normal force coefficients C_nM^2, the tangential force coefficient C_tM^2, and the pitching moment coefficient C_mM^2 are delivered to S4, where the lower 10/rev harmonics of the CFD air loads are extracted.

The difference in air loads between S4 aerodynamics and FLOWer aerodynamics are added to the next S4 trim, resulting in new blade deformations and updated rotor control angles of the 1^{st} iteration. This sequence of S4 and FLOWer computations is repeated until the variation of the rotor control angles falls below a user-defined threshold. The weak coupling procedure provides trimmed solutions for rotors taking into account the elastic blade deformations, the viscous effects and the influence of the 3D blade tip flow field.

No blade-vortex-interaction is modelled within FLOWer since the vortex conservation is not granted in the grids and numerical schemes. However, all air loads above 10/rev are retained within S4, thus keeping BVI phenomena using its prescribed wake model. In this work, the above described weak-coupling approach was applied to the passive and the active twist rotors in the same manner.

2.4. Computational Setup

The basic setup and the geometrical size of the computational mesh used for the CFD calculations are shown in Figure 1. The surface of the rotor blade is discretized with 85 cells in the radial direction, and 162 cells are used for the discretization of the sectional airfoil geometry. A detailed view of the blade grid setup is given in Figure 2. The blade grids are embedded via the Chimera technique in a background grid which consists of Cartesian blocks with hanging nodes. The distribution of the grid points are summarized in Table 1.

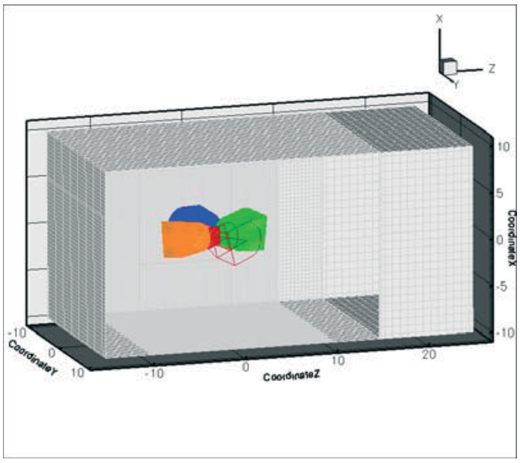

Figure 1: Overview of the grid setup

	No. of blocks	No. of points
Blades (x 4)	10	1,143.254
Background	36	2,014.320
Total		6,587.336

Table 1: Grid parameters

The blade deformation is achieved by taking advantage of an existing FLOWer module which has been developed by IAG [14] for the weak-coupling procedure between FLOWer and the EUROCOPTER flight mechanics tool HOST [15]. The output data of the DLR rotor code S4 for FLOWer concerning the rotor control angles and the blade deformation are converted into a HOST-conform format and read in by FLOWer with the deformation module. The effect of applying the deformation module is shown in Figure 3, in which the original blade geometry (grey) and the deformed blades (blue) are shown.

In order to ensure that the blade behaviour is correctly represented in the flow solver, the flap deflections at the c/4-line at four radial positions (Figure 4), as well as the resulting pitch control and the elastic torsion angles at r/R = 0.94 (Figure 5) are compared between S4 and FLOWer. As can be seen from Figure 4 and Figure 5, the blade deformations prescribed by S4 are correctly reproduced by the CFD solver. The difference between both codes concerning the flap deflection at the blade tip (r/R = 1) occurs due to an anhedral in the elastic axis starting at the initial radius of the parabolic tip and extending up to the blade tip. This vertical displacement lowering the flap deflection at that time was not considered within the output routine of S4 but within FLOWer, such that the flap deflection computed by S4 is a little higher.

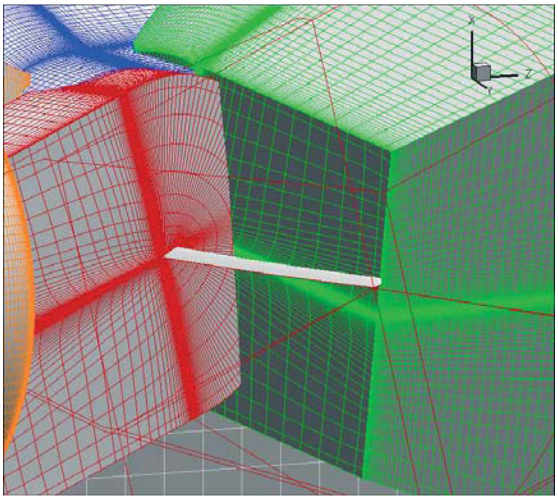

Figure 2: Detail view of the deformed blade geometry

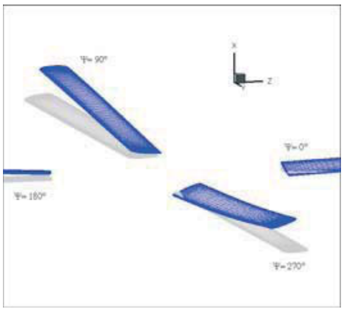

Figure 3: Blade geometry in flow solver after applying the deformation tool

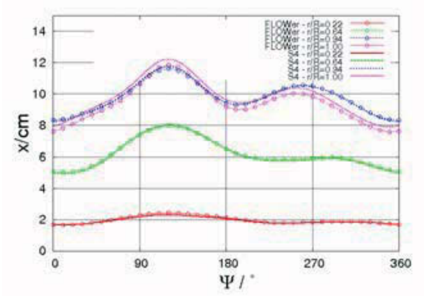

Figure 4: Flap deflections of the blade at different radial positions (r/R = 0.22, 0.64, and 0.94,1), TC1

However, differences in the simulation results because of the anhedral are assumed to be negligible. All time histories are presented for a radial position of 0.94R, which is the last radial position before the parabolic tip starts, to assure that the results of the coupling procedure are directly comparable.

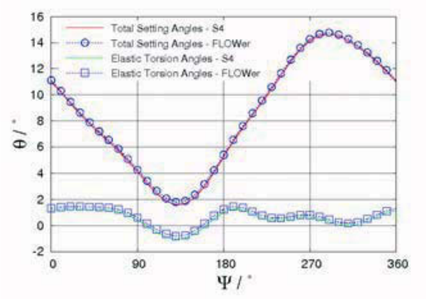

Figure 5: Pitch angle and elastic torsion angles of the blade at r/R = 0.94, TC1

2.5. Test Case Description

All coupled benefit computations presented in this paper have been performed for the FRIENDCOPTER model rotor blade design which is based on a Mach scaled Bo105 model rotor with a radius of R = 2m and a pre-twist of -8°/R. To adopt the blade design to a more advanced rotor blade, two different airfoils have been considered. Within the spanwise range of 0.22 ≤ r/R ≤ 0.75, a NACA23012 airfoil has been chosen while in the outer part, starting at 0.9R, an OA209 airfoil has been selected. The intersection area between both airfoils has been morphed linearly whereas the blade chord of c/R = 0.0605 remains constant. Additionally, starting at a radial position of r/R = 0.95, the blade is equipped with a parabolic tip.

The active twist is generated by 2x7 Macro Fiber Composite (MFC) actuators which are integrated into the upper and lower blade skin. The area of the FRIENDCOPTER model blade covered by MFC actuators ranges 0.22 ≤ r/R ≤ 0.94.

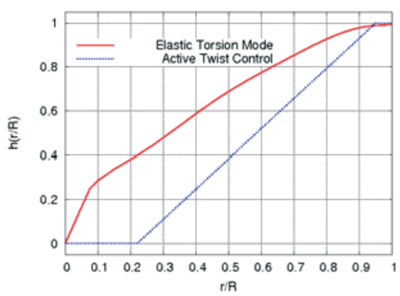

Figure 6: Modelling of the active twist control

The FRIENDCOPTER model rotor blade without active twist control is denoted as the passive rotor while the with active twist control it is referred to as the active rotor. For the CFD simulation, the torsional deformation induced by the active twist control is achieved with an additional active twist control mode shape, which takes effect only for the radial range of 0.22 ≤ r/R ≤ 0.94 (the actuator area). The active twist control mode shape is assumed to be zero at the inner radius of the active area, increasing linearly to the value of one at the outer radius of this area. Beyond the outer radius, the active twist control mode shape keeps the value of one up to the blade tip. In Figure 6, the mode shape of the first elastic torsion mode and of the active twist control mode is plotted.

For the benefit studies with regard to power consumption, vibration and noise, coupled computations have been performed for test cases TC1 and TC2, whose flight and trim parameters are summarized in Table 2. In both cases, the calculations were trimmed for thrust, roll and pitch moment by adaptation of the control angles θ_0, θ_{1c} and θ_{1s}, while the rotor shaft angle has been kept fixed for each case.

Parameter	Symbol	Unit	TC1	TC2
Free stream air speed	V_∞	m/s	69.8	82.3
Free stream Mach number	M_∞	-	0.200	0.239
Tip Mach number	M_{tip}	-	0.646	0.640
Advance ratio	μ	-	0.318	0.378
Blade loading coefficient	C_T/σ	-	0.069	0.060
Shaft angle	α_{sh}	deg	-9.10	-8.11
Precone angle	β_P	deg	2.5	2.5

Table 2: Flight and trim parameters

2.6. Control laws and their objectives

The general form of higher harmonic control laws reads

$$\theta(t) = \theta_0 + \sum_i \theta_i \cos(i\psi - \psi_i) \qquad (2)$$

with $\psi = \Omega t$ as non-dimensional time (= azimuth), where Ω = 109 rad/s is the constant rotational frequency of the rotor and t is the time. For test case TC1 the objective is vibration reduction using control frequencies from 2-5/rev. The result generated by S4 is shown in (Figure 7).

For TC2 (high speed) the objective is power reduction. Wind tunnel experiments using HHC [16], IBC [17], and flight tests [18] have shown that a 2/rev control input is best suited to achieve performance enhancements for rotors operating at high speeds. The resulting 2/rev control law generated by S4 is shown in (Figure 8).

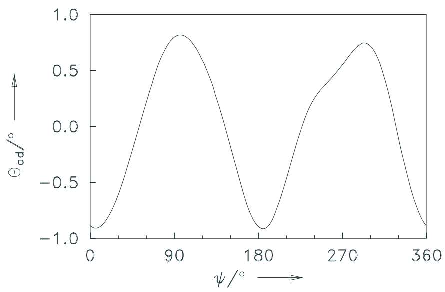

Figure 7: Multi-harmonic control law for TC1 with θ_2=0.83°, ψ_2=197°, θ_3=0.08°, ψ_3=260°, θ_4=0.11°, ψ_4=177°, θ_5=0.05°, ψ_5=68°

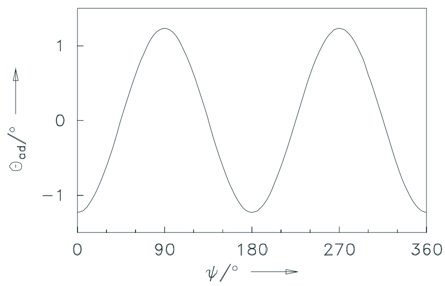

Figure 8: Control law for TC2 with θ_2=1.25°, ψ_2=180°

3. RESULTS

In this section, the results of the coupled S4/FLOWer calculations are presented and discussed. Passive and active rotors are compared for the two test cases explained above. Additionally, the changes in the simulation results obtained by the coupling of both computational codes are presented.

3.1. Test Case 1

The pressure distributions on the upper blade surface for test cases TC1 are compared qualitatively in Figure 9. Typical features of a rotor in fast forward flight are visible such that a pronounced low pressure area in the outer radial region exists on the front blade (ψ = 180°). On the retreating side (ψ = 270°), higher cp values indicate that an area of reversed or separated flow exists. From the differences in the pressure distribution one can see, that these areas are obviously smaller for the active rotor. By applying the active twist control, the extensive low pressure region apparent on the blade at ψ = 180° is reduced significantly.

The iteration history of the control angles for the passive and the active rotor are given in Figure 10. For both cases, a trimmed condition is obtained very quickly within four iteration steps, with only marginal variations thereafter.

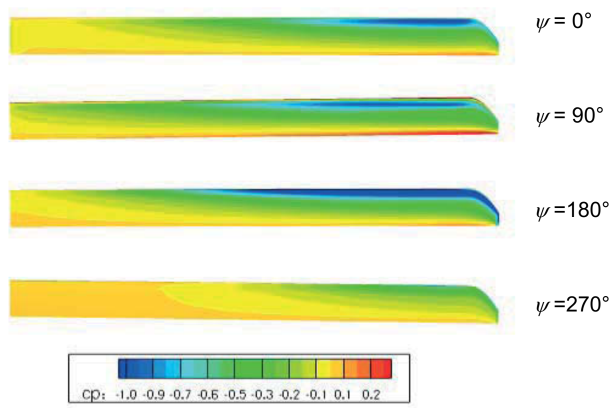

(a) passive rotor

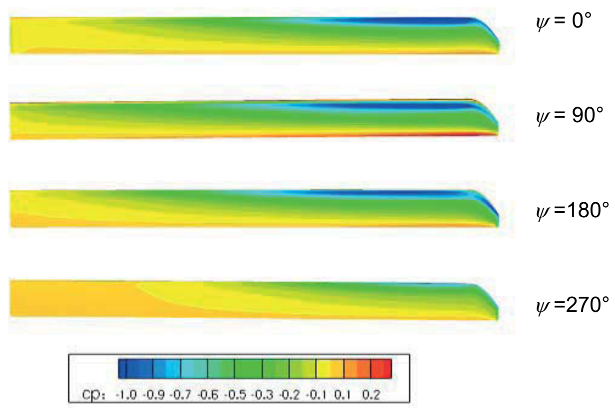

(b) active rotor

Figure 9: Upper surface pressure distribution of test case TC1

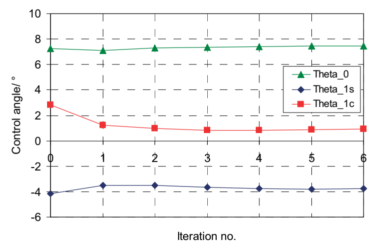

(a) passive rotor

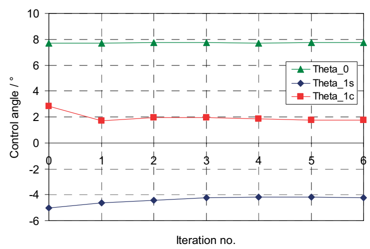

(b) active rotor

Figure 10: Rotor trim for test case TC1

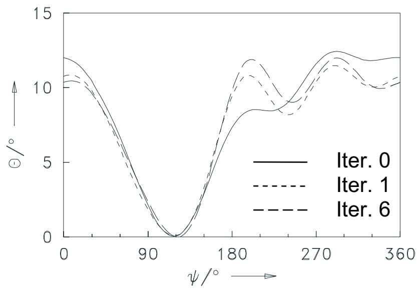

(a) passive rotor

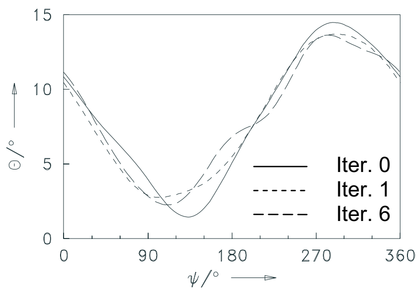

(b) active rotor

Figure 11: Pitch angle for different iteration steps, 0.94R, TC1

Figure 11 shows a comparison of the total pitch angle (control plus torsion) at r/R = 0.94 for the passive and the active rotor at different iteration steps. Step 0 (solid line) represents the isolated S4 results, step 1 (short dash) describes the first coupling and step 6 (long dash) provides the results for the final rotor trim condition. For the passive rotor (Figure 11a), a clear change in pitch angle can be seen for coupled computations on the retreating side, where due to CFD aerodynamics a stronger dynamic response in torsion can be observed. On the advancing side, changes resulting from the CFD aerodynamics are only marginal, indicating a strong similarity of S4 and CFD air loads in this area. Basically, the amplitudes are slightly decreased for step 1 and 6 except for the azimuthal area around ψ = 180° where the resulting pitch angle is increased. Also with an applied active control (Figure 11b), the amplitudes are smaller for the coupled simulation. Additionally, a shift to smaller azimuth positions can be seen for the pitch angle on the advancing side compared to the uncoupled S4 computations.

For the passive case higher harmonic torsion response can be found especially on the retreating side. These higher harmonic contents diminish, applying the active control. Thus, a significant 1/rev content in the pitch angle is apparent for the active rotor. The magnitudes on the advancing side are reduced but they are enlarged on the retreating side compared to the passive case.

An illustration of the normal force coefficients is given in Figure 12. For the passive rotor, uncoupled and coupled results are in good agreement. As explained before, the pitch angle is subject to a major change for the passive rotor in the area of ψ = 180° caused by the introduction of the FLOWer aerodynamics (Figure 11). Nevertheless, only a small increase in the normal force coefficient can be seen in Figure 12. Thus, the effect of the pitch angle regarding to the normal force coefficient is not significant.

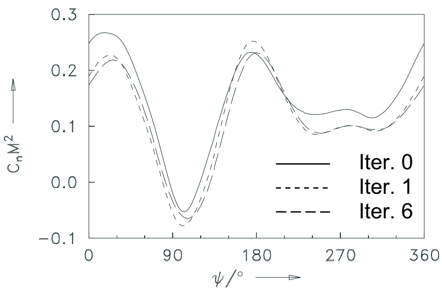

(a) passive rotor

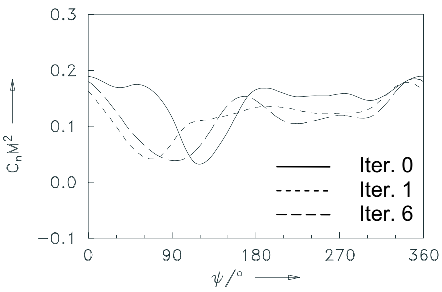

(b) active rotor

Figure 12: Comparison of C_nM^2 for different iteration steps, low-pass-filtered, 0.94R, TC1

Employing CFD aerodynamics, the dynamics in the normal force coefficient are altogether lowered and again a shift to smaller azimuth angles can be seen in the time histories between coupled and uncoupled computations in Figure 12.

The normal force coefficient distribution within the rotor disk is shown in Figure 13 for uncoupled and coupled simulations as well as for the passive and the active rotor. A more uniform distribution corresponding to the passive rotor is obtained implementing the CFD aerodynamics. At the advancing side, areas with negative lift gain an increase in their extension while at the retreating side those areas are enlarged inboard of the blade within the reversed flow area (see Figure 13a and Figure 13b).

The results for uncoupled (Figure 13c) and coupled computations (Figure 13d) for the active case differ in a clockwise shift. Furthermore, areas of the highest C_nM^2 values are more concentrated with FLOWer aerodynamics. Under the influence of the active twist control, areas with negative lift are eliminated at the advancing side. This leads to a more uniform C_nM^2 distribution over the rotor disk compared to the passive case and can be assumed as most important for the estimated vibration reduction.

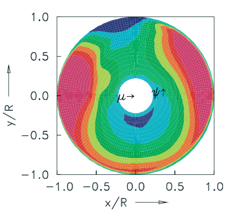

(a) passive rotor, uncoupled, iter. 0

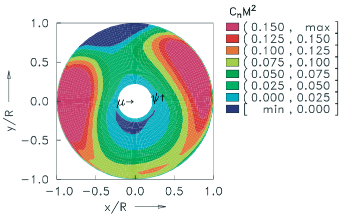

(b) passive rotor, coupled, iteration 6

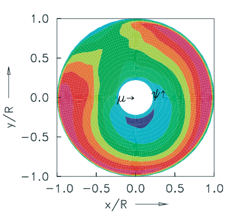

(c) active rotor, uncoupled, iter. 0

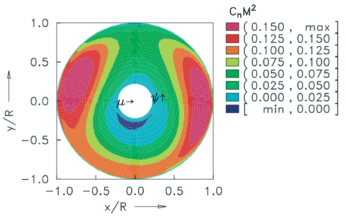

(d) active rotor, uncoupled, iteration 6

Figure 13: Comparison of C_nM^2 distribution in the rotor disk, low-pass-filtered, TC1

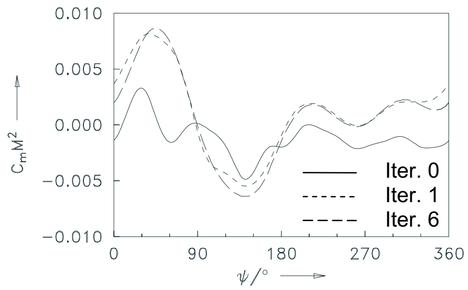

(a) passive rotor

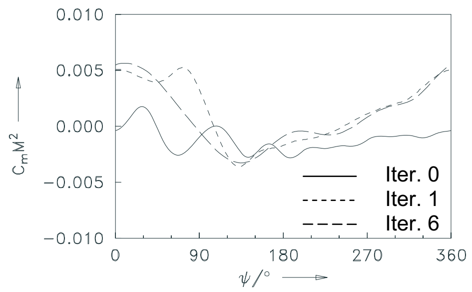

(b) active rotor

Figure 14: Comparison of C_mM^2 for different iteration steps, low-pass-filtered, 0.94R, TC1

Operating the active control law leads to a decrease in the moment coefficients C_mM^2 in Figure 14. It is clearly noticeable that higher harmonic contents (still below 10/rev) as predicted by S4 aerodynamics especially on the advancing side are not predicted by the CFD aerodynamics for both, passive and active rotor. In general, an increase in magnitude of the lower harmonic content can be found for C_mM^2 due to the introduction of the FLOWer aerodynamics. Basically, the moment coefficient is stronger influenced by 3D flow field effects than the normal force coefficient. 3D effects are enlarged with increasing radius such that differences between CFD and S4 aerodynamics become more apparent towards the blade tip.

Concluding, an important change in the moment coefficient can be found as the major difference between coupled and uncoupled computations, significantly influencing the torsional response of the blade. Although a clear increase in the pitch angle around ψ = 180° is obtained for the passive case applying CFD aerodynamics, while no significant effect on the normal force coefficient is resulting in this azimuthal area. For the active twist control applied, small alterations in the pitch angle resulting from the CFD aerodynamics seem to have an important impact on the normal force coefficient.

The blade motion in flapping is illustrated in Figure 15 for both passive and active rotor as well as for different iteration steps. Coupled and uncoupled simulation results are in good agreement for the passive case, although the magnitude is varying slightly and a small shift to larger azimuth angles is computed on the advancing side.

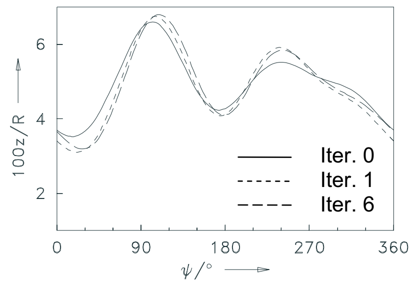

(a) passive rotor

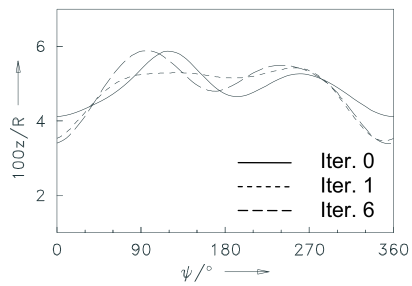

(b) active rotor

Figure 15: Flapping motion for different iteration steps, low-pass-filtered, 0.94R, TC1

Variations resulting from CFD aerodynamics are more apparent for the active rotor. The shift in the time histories of the flapping motion for the coupled simulations is in contrary direction as for the passive case. Although differences in magnitude are visible, the curve shape basically looks quite similar to the S4 results without CFD aerodynamics.

Due to the importance of the elastic torsion concerning the effectiveness of an active control, the influence of 3D aerodynamic effects has been analysed, see Figure 16. Main differences between coupled and uncoupled simulations can be found for the amplitudes and phases of the elastic torsion. While a minor shift of the time histories to larger azimuth positions is visible for the passive case, a clear shift to smaller azimuths is computed for the active case. The dynamics regarding the torsional blade response are smaller for the active case employing CFD.

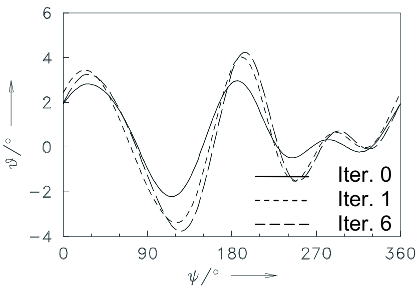

(a) passive rotor

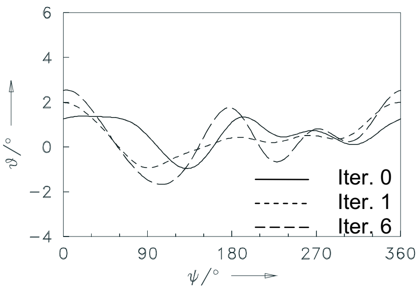

(b) active rotor

Figure 16: Elastic torsion for different iteration steps, low-pass-filtered, 0.94R, TC1

Since the applied control law has been optimised to minimum vibration, the quality criterion QC_v is subject to the benefit analysis first. The criterion QC_v is determined from the 4/rev force and moment components in the non-rotating frame since these components represent the source for vibration excitation of the helicopter airframe.

(3)

$$QC_v = \sqrt{\frac{F^2_{x,4/rev} + F^2_{y,4/rev} + F^2_{z,4/rev}}{N} + \frac{M^2_{x,4/rev} + M^2_{y,4/rev}}{Nm}}$$

Table 3 summarizes the quality criteria computed for the passive and the active rotor as well as for the uncoupled simulation (iteration step 0) and the trimmed condition of the coupling S4/Flower procedure (iteration step 6). The quality criterion is referenced to the corresponding criteria of the passive case.

Quality criteria	uncoupled	S4+Flower
$QC_v / QC_{v,0}$	0.06	0.16

Table 3: Comparison of noise and vibration quality criteria, TC1

Applying the active control law, vibrations can be reduced to 6% of the value of the passive rotor in an uncoupled condition (S4 alone), while a reduction to 16% is found for the coupled simulations. This effect can be explained by the more advanced FLOWer aerodynamics which, as explained before, fully account for 3D effects like a blade tip flow field.

Although the optimisation for test case TC1 was aiming to minimize vibration, minor savings in rotor power are apparent according to Figure 17 which is not surprising since the control laws for TC1 (vibration reduction, Figure 7) and TC2 (power reduction, Figure 8) are very similar. Comparing uncoupled and coupled computations, higher power gains are obtained considering advanced 3D aerodynamics.

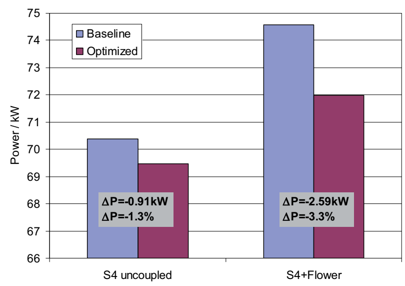

Figure 17: Comparison of power reduction, TC1

Resulting, a power reduction of 1.3% is obtained by the S4 simulation due to the active twist control, while the FLOWer aerodynamics enhance the prediction up to 3.3% power reduction.

3.2. Test Case 2

For the test case TC2, the pressure distributions on the blade upper surface shows similar patterns as TC1 in Figure 9. Akin to the test case TC1, by applying the active twist control, the extensive low pressure region apparent on the blade at ψ = 180° is reduced significantly (see Figure 18).

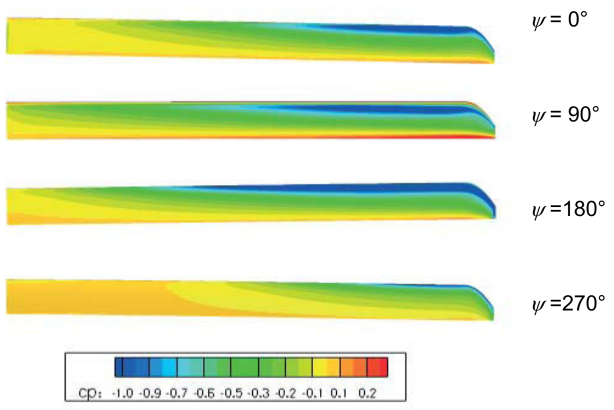

(a) passive rotor

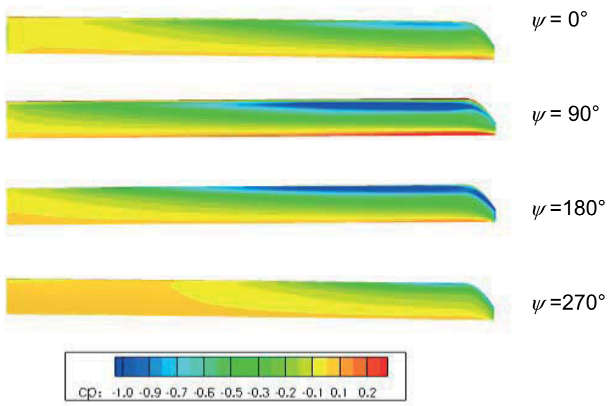

(b) active rotor

Figure 18: Upper surface pressure distribution of test case TC2

For test case TC2, BVI can be detected in the azimuthal area around ψ = 90° for the passive case. Figure 19 shows a comparison of the 10/rev high-pass-filtered normal force coefficient for the passive rotor and different iteration steps. Since BVI is a high-frequency event which alters the blade pressure distribution and therefore the lift distribution on the blade, areas with maximum high-pass-filtered normal force coefficient indicate BVI locations in the rotor disk. Due to the lower disk loading of test case TC2 (C_T/σ = 0.06, α_{sh} = -9.1) and the shaft angle of attack being 1° more positive compared to test case TC1 (C_T/σ = 0.069, α_{sh} = -8.11), vortices are convected downwards more slowly. Resulting, blade tip vortices stay within the rotor plane for a longer time such that they are able to counteract with the following rotor blades.

Introducing the FLOWer aerodynamics, a change in the flight path of the vortices is achieved such that blade vortex interactions are eliminated. These different rotor conditions could not be stabilized during the trim procedure of the coupled computations such that no trimmed condition could be reached for the passive case (Figure 20(a)). Introducing the active control generates a significant change in the aerodynamics of the rotor and leads to a stable trim condition very quickly (Figure 20(b)).

While for iteration step 0 hardly BVI can be detected, iteration step 1 and 2 show rather large areas with BVI at ψ = 90°. In contrast, iteration 3 shows no BVI at all. Comparing Figure 19(a-d) and Figure 19(e-h) obviously a repetition of the aerodynamic conditions of iteration 0-3 is included in iteration 4-7.

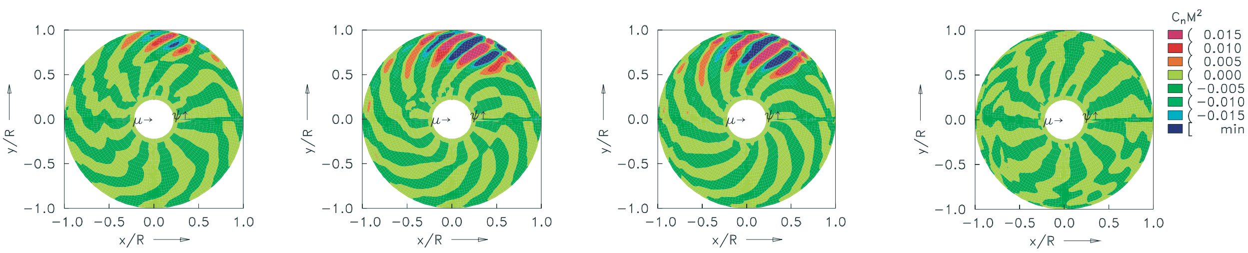

a) iteration 0 b) iteration 1 c) iteration 2 d) iteration 3

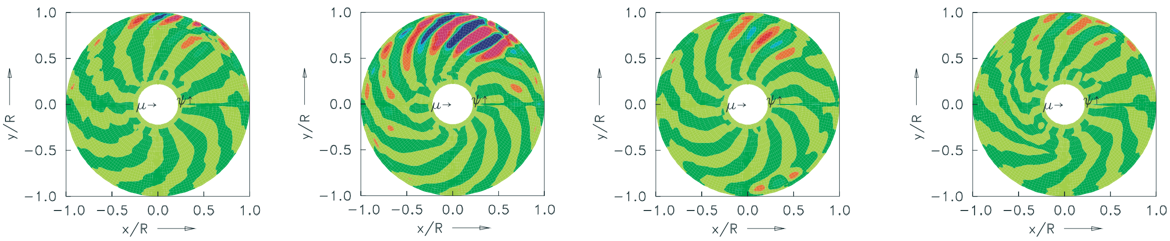

e) iteration 4 f) iteration 5 g) iteration 6 h) iteration 7

Figure 19: BVI locations indictated by the 10/rev high-pass-filtered C_nM^2 coefficient , passive rotor

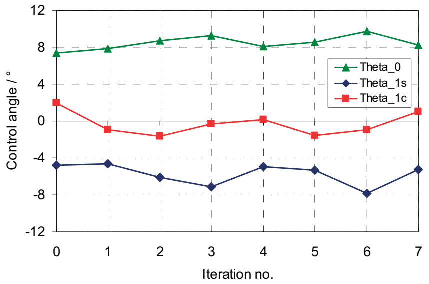

(a) passive rotor

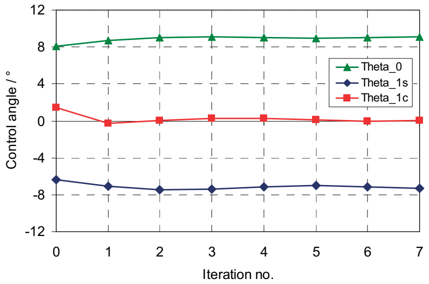

(b) active rotor

Figure 20: Rotor trim for test case TC2

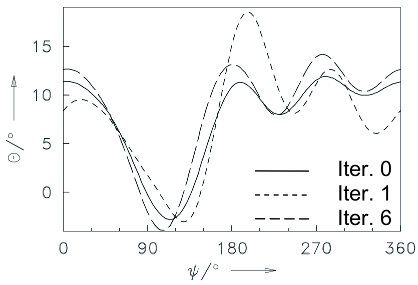

(a) passive rotor

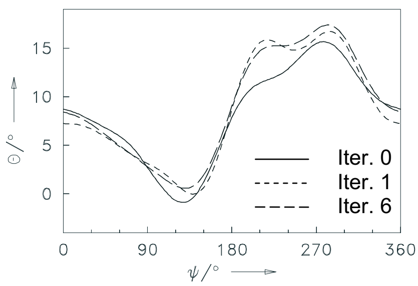

(b) active rotor

Figure 21: Pitch angle for different iteration steps, 0.94R, TC2

Figure 21(a) and Figure 21(b) show a comparison of the pitch angles applied for the passive as well as the active case. In contrast to test case TC1 where a better agreement between uncoupled and coupled simulations has been present for the active case, differences are more significant for the passive case for test case TC2. Nevertheless, the uncoupled and coupled computation results correspond quite well.

Good agreement between uncoupled and coupled results is also visible for C_nM^2 in Figure 22. For the passive case, a shift of the time histories to smaller azimuth angles is resulting from the integration of the CFD aerodynamics, while time histories of C_nM^2 for the active case show a contrary behaviour. These shifts in the time histories are effective in opposite direction to test case TC1 for both passive and active case.

While for the passive case the amplitudes of C_nM^2 are increased, they are decreased for the active case comparing uncoupled and coupled results. Using an active twist control, the lift coefficients are lowered on the advancing such that maximum lift coefficients are shifted to higher azimuth angles compared to the passive case.

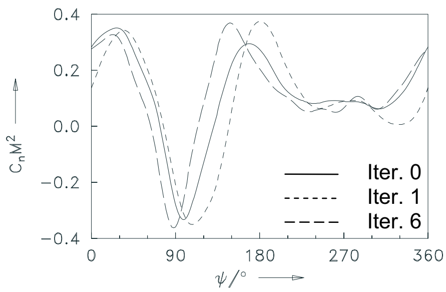

(a) passive rotor

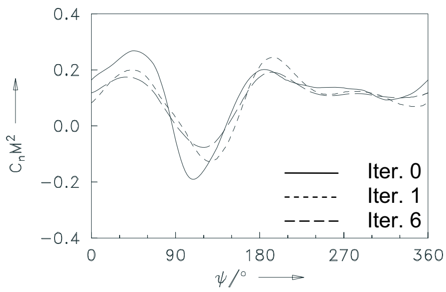

(b) active rotor

Figure 22: Comparison of C_nM^2 for different iteration steps, low-pass-filtered, 0.94R, TC2

An illustration of the normal force coefficient over the rotor disk is given in Figure 23. It is obvious that operating the active twist control diminishes the dimensions of areas with negative lift outboard of the blade on the advancing side. On the retreating side, the lift coefficient is enhanced at the blade tip which results in an important reduction of the power consumption of the rotor. The effects on lift distribution over the rotor disk can be found even more clearly for the coupled computations. For the passive case, areas with negative lift are determined to be larger on both, advancing and retreating side. But the influence of the twist control on the lift distribution is the same as for the uncoupled simulation.

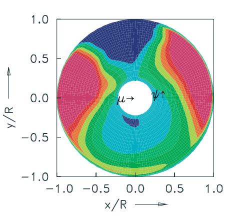

(a) passive rotor, uncoupled, iter. 0

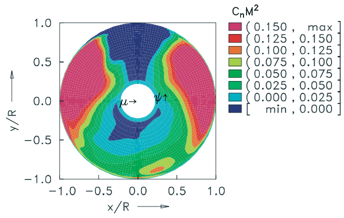

(b) passive rotor, coupled, iteration 7

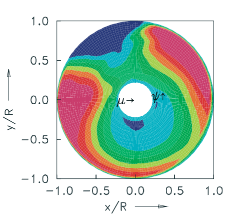

(c) active rotor, uncoupled, iter. 0

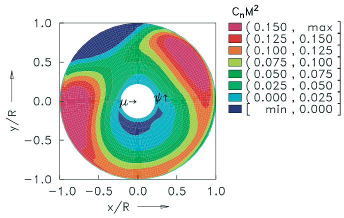

(d) active rotor, coupled, iteration 7

Figure 23: Comparison of C_nM^2 distribution over rotor disk, low-pass-filtered, TC2

The moment coefficients calculated for test case TC2 (Figure 24) show higher dynamics than those determined for TC1. It is noteworthy that for the passive case higher harmonic contents are also contained within the FLOWer aerodynamics. These result from increased blade dynamics in flapping and torsion motion (Figure 25, Figure 26) compared to test case TC1 (Figure 15, Figure 16).

The negative peak in the moment coefficient around an azimuth angle of 75° is enhanced for the application of the active twist control. Replacing the low-frequency aerodynamics of S4 by the CFD aerodynamics leads to a tremendous change in the moment coefficient within this azimuthal area. As explained for test case TC1, the moment coefficient is increasingly influenced by 3D effects approaching the blade tip. Those 3D effects are not accounted for by the 2D aerodynamics of S4. But again, the agreement between uncoupled and coupled computations is good on the retreating side for the active case where a trimmed condition could be reached.

The time histories of the flapping motion visible in Figure 25 vary quite strong for the passive case and different iteration steps on the advancing side due to non-convergence of the solution. For the active case (Figure 25b), results for the flapping motion show good agreement for uncoupled as well as coupled simulations. Again, the magnitude of the deflections compared to the passive case are reduced, mainly at the advancing side.

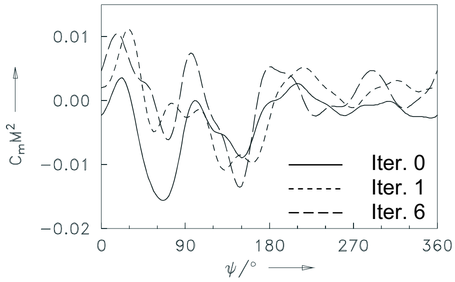

(a) passive rotor

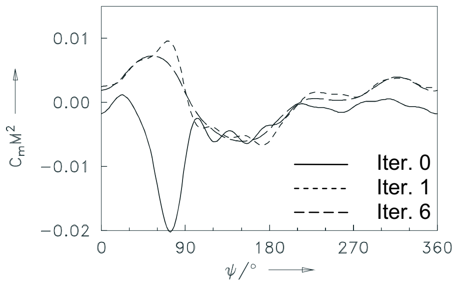

(b) active rotor

Figure 24: Comparison of C_mM^2 for different iteration steps, low-pass-filtered, 0.94R, TC2

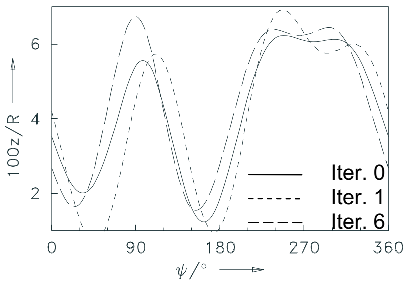

(a) passive rotor

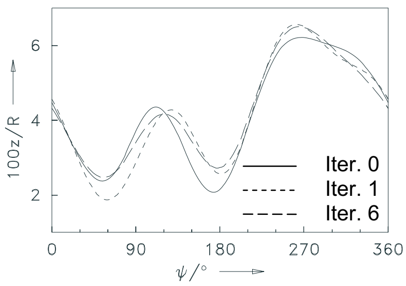

(b) active rotor

Figure 25: Flapping motion for different iteration steps, low-pass-filtered, 0.94R, TC2

A similar trend as for the flapping motion can be noted for the elastic torsion from Figure 26. Comparing passive and active case as well as the results with and without coupling procedure, time histories look very similar and most of all differ in magnitude.

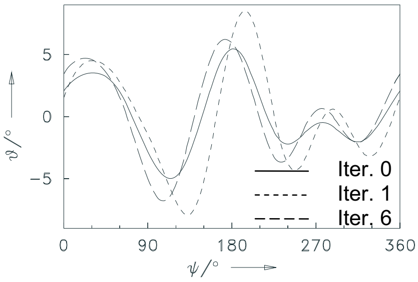

(a) passive rotor

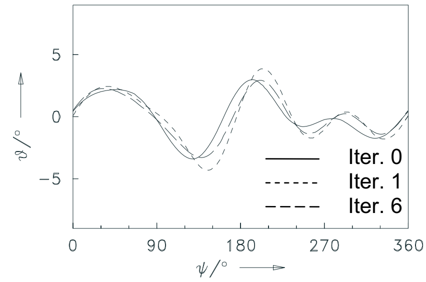

(b) active rotor

Figure 26: Elastic torsion for different iteration steps, low-pass-filtered, 0.94R, TC2

Although the control law applied to test case TC2 was optimised to minimum power consumption, the quality criteria for vibration are provided by Table 4 for benefit analysis. It is obvious that the active twist control also leads to a high decrease in the vibration quality criteria. This effect is not surprising since for test case TC1, mainly a 2/rev control was identified by the optimisation to be best suited for vibration reduction and both test cases are quite similar to each other.

Quality criteria	uncoupled	S4+Flower
$QC_v / QC_{v,0}$	0.57	0.19

Table 4: Comparison of noise and vibration quality criteria, TC2

Uncoupled simulation runs provide power savings of 7% comparing passive and active case and are somewhat higher than for test case TC1. A tremendous power reduction is gained for the coupled computations but one has to keep in mind that the magnitude of the power strongly varied for each iteration step of the trim procedure.

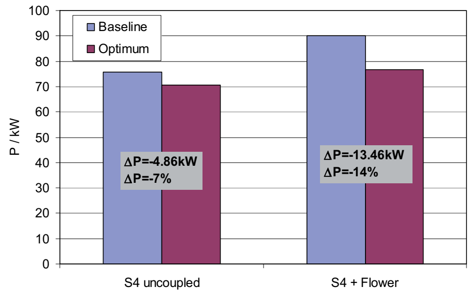

Figure 27: Comparison of power reduction computed for passive and active case as well as coupled and uncoupled simulations, TC2

Since no trimmed condition could be reached, the value of the passive rotor for power is as unsure as it was for the quality criteria. As it can be seen from Figure 28, the power consumption is changing strongly with each iteration step for the passive rotor while for the active rotor it has converged with the second iteration step. Resulting, no reliable statement about the power gain concerning the use of the active control can be given.

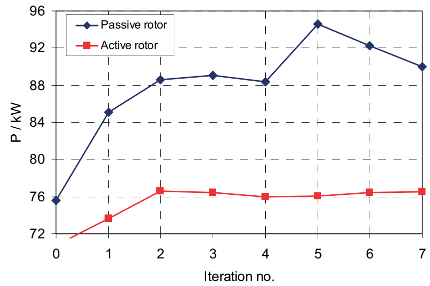

Figure 28: Comparison of the power consumption for different iteration steps, passive and active rotor

However, since test case TC2 is similar to TC1, the improvements in power consumption should be of similar magnitude for both cases such that a power gain of 14% probably is too high. Additionally, it has to be mentioned that FLOWer tends to overestimate power savings. For example, blade stubs were not gridded for this investigation and also the effect of transition from laminar to turbulent boundary layer was not considered in the computation. These effects would reduce the rotor power by several percents [19][20].

4. CONCLUSIONS

Computational simulations have been conducted to evaluate the potential gain with respect to vibration reduction and performance enhancement by applying the active twist control to a model rotor blade. The studied rotor configuration is a model rotor defined in the framework of the European FRIENDCOPTER project. A weak coupling method between the CFD code FLOWer and the rotor simulation code S4 was applied to the isolated rotor configuration, so that trimmed CFD/CSM results could be obtained for two forward flight test cases.

In the first test case, the focus was put on the vibration reduction. In this case, the weak-coupled simulations showed that a vibration reduction of 84% could be achieved applying the active twist control law (Figure 7). In the second test case, a power reduction was aimed by applying the active control law. The reduction of the power consumption was estimated to be 14%. This value of the power reduction is probably overestimated, since BVI phenomena appeared in the coupled simulation of the passive rotor which caused convergence problems for the reference case. Nevertheless, the numerical results showed clearly that the application of an active twist control leads to an improvement in rotor performance regarding vibration and power consumption aspects. Further investigations are needed toward the blade design and the optimization of the active twist control laws.

ACKNOLEDGEMENTS

The authors would like to thank the FRIENDCOPTER consortium for its funding for this study.

REFERENCES

[1] CESNIK, C.E.S., SHIN, S., WILKIE, W.K., WILBUR, M., MIRICK, P.H.: “Modeling, Design and Testing of the NASA/ARMY/MIT Active Twist Rotor Prototype Blade”, 55th Annual Forum of the American Helicopter Society, Montreal, Canada, 1999

[2] SHIN, S., CESNIK, C.E.S., HALL, S.R.: “Closed-Loop Control Test of the NASA/ARMY/MIT Active Twist Rotor for Vibration Reduction”, 59th Annual Forum of the American Helicopter Society, Phoenix, Arizona, USA, 2003

[3] DIETERICH, O., ENENKL, B., ROTH, D.: “Trailing Edge Flaps for Active Rotor Control Aeroelastic Characteristics of the ADASYS Rotor System”, 62nd Annual Forum of the American Helicopter Society, Phoenix, Arizona, USA, 2003

[4] ROTH, D.: “Active Rotor Control by Flaps for Vibration Reduction – Full Scale Demonstrator and First Flight Test Results –“, 32nd European Rotorcraft Forum , Maastricht, Netherlands, 2006

[5] STRAUB, F.K., ANAND, V.R., BIRCHETTE, T.S., LAU, B.H.: “Wind Tunnel Test of the SMART Active Flap Rotor”, 65th Annual Forum of the American Helicopter Society, Grapevine, Texas, USA, 2009

[6] RIEMENSCHNEIDER, J., WIERACH, P., OPITZ, S., HOFFMANN, F.: “Testing and Simulation of an Active Twist Rotor Blade”, Adaptronic Congress, Göttingen, Germany, 2007

[7] HOFFMANN, F., OPITZ, S., RIEMENSCHNEIDER, J.: “Validation of Active Twist Modeling Based on Whirl Tower Tests”, 65th Annual Forum of the American Helicopter Society, Grapevine, Texas, USA, 2009

[8] VAN DER WALL, B. G.: “An Analytic Model of Unsteady Profile Aerodynamics and its Application to a Rotor Simulation Program”, 15th European Rotorcraft Forum, Amsterdam, Netherlands, 1989

[9] BEDDOES, T.S. : “A Wake Model for High Resolution Airloads”, International Conference on Rotorcraft Research, Research Triangle Park, NC, USA, 1985

[10] VAN DER WALL, B.G. : “The Effect of HHC on the Vortex Convection in the Wake of a Helicopter Rotor”, Aerospace Science and Technology, Vol. 4, No. 5, p. 320-336, 2000

[11] KROLL, N., EISFELD, B., BLEEK, H.M.: “The Navier-Stokes Code FLOWer”, Vol. 71 of Notes on Numerical Fluid Mechanics, pages 58-71. Vieweg, Braunschweig, 1999

[12] JAMESON, A.: “Time Dependent Calculation Using Multigrid, with Applications to Unsteady Flows Past Airfoils and Wings”, AIAA-Paper 91-1596, 1991

[13] SCHWARZ, T.: “The Overlapping Grid Technique for the Time Accurate Simulation of Rotorcraft Flows”, 31st European Rotorcraft Forum, Florence, Italy, 2005

[14] DIETZ, M., KRÄMER, E., WAGNER, S., ALTIMIKUS, A.: “Weak Coupling for Active Advanced Rotors”, 31st European Rotorcraft Forum, Florence, Italy, 2005

[15] BENOIT, B., DEQUIN, A.-M., KAMPA, K., VON GRÜNHAGEN, W., BASSET, P.-M., AND GIMONET, B.: “HOST: A General Helicopter Simulation Tool for Germany and France”, 56th Annual Forum of the American Helicopter Society, Virginia Beach, Virginia, USA, 2000

[16] SHAW, J., ALBION, N., HANGER, E.J., JR., TEAL, R.S.: “Higher Harmonic Control: Wind Tunnel Demonstration of Fully Effective Vibratory Hub Force Suppression”, 41st Annual Forum of the American Helicopter Society, Fort Worth, Texas, USA, 1985

[17] JACKLIN, S.A., NGUYEN, K.Q., BLASS, A., RICHTER, P.: “Full-Scale Wind Tunnel Test of a

Helicopter Individual Blade Control System", 50th Annual Forum of the American Helicopter Society, Washington D.C., 1994

[18] KEßLER, C.: "Open Loop Flight Test Results and Closed Loop Status of the IBC System on the CH-53G Helicopter", 59th Annual Forum of the American Helicopter Society, Phoenix, Arizona, USA, 2003

[19] PAHLKE, K., VAN DER WALL, B.G.: "Progress in Weak Fluid-Structure-Coupling for Multibladed Rotors in High-Speed Forward Flight", 28th European Rotorcraft Forum, Bristol, Great Britain, 2002

[20] PAHLKE, K., VAN DER WALL, B.G.: "Chimera Simulations of Multibladed Rotors in High-Speed Forward Flight with weak fluid-structure coupling", In: *Aerospace Science and Technology*, Vol. 9, No. 5, 2005, pp. 377-389NAME : "Title", Journal/Books, City, year1989